Eur. Phys. J. Special Topics **229**, 331–346 (2020)

https://doi.org/10.1140/epjst/e2019-900085-0

THE EUROPEAN PHYSICAL JOURNAL SPECIAL TOPICS

Regular Article

MHD convection of nanofluid in porous medium influenced by slanted Lorentz force

S. Sureshkumar[1], S. Muthukumar[2], M. Muthtamilselvan[3,a], Deog-Hee Doh[4], Gyeong-Rae Cho[4], and Eswari Prem[5]

[1] Department of Mathematics, Kongu Engineering College, Perundurai 638052, India
[2] Department of Mathematics, K.S.Rangasamy College of Technology, Tiruchengode 637215, India
[3] Department of Mathematics, Bharathiar University, Coimbatore 641046, India
[4] College of Engineering, Division of Mechanical Engineering, Korea Maritime and Ocean University, Busan 606–791, South Korea
[5] P.G. and Research Department of Mathematics, Government Arts College for Men, Krishnagiri 635001, India

Received 15 May 2019 / Received in final form 8 July 2019
Published online 11 February 2020

Abstract. This paper presents a numerical investigation on magneto-hydrodynamics combined convection in a nanofluid-saturated porous 2-D cavity with different tilting angles of applied magnetic field and aspect ratios. The moving upper horizontal wall is heated uniformly. The temperature along the bottom wall is a constant cold temperature while the adiabatic condition is maintained at the vertical sidewalls. The finite volume method is applied to solve the system of non-dimensional equations. The pertinent parameters of the current study are Hartmann number (Ha), solid volume fraction (χ), Richardson number (Ri), the aspect ratio (Ar), Darcy number (Da), and the inclination angle of the magnetic field (γ). The slope of applied magnetic field affects the magnetic field intensity and the overall rate of heat transfer is augmented in the forced convection regime than the mixed convection regime. The mean Nusselt number raises on increasing of Ar for all considered Richardson numbers. In the presence of magnetic field, the rate of heat transfer is almost equal to the amplification of solid volume concentration when $Ar = 0.25$, whereas, it increases for $Ar > 0.25$ with the raise in the solid volume concentration. An increase in Hartmann number and Darcy number is insignificant on mean rate of heat transfer in the mixed convection regime at $Ar \leq 0.5$.

1 Introduction

Magneto-hydrodynamics (MHD) is the analysis of physical behavior of fluids conducting with electromagnetic field. MHD convective heat transfer analysis in a cavity is one of the most extensively referred studies in the field of thermo-fluids for the last few decades as it finds numerous applications in electromagnetic casting, crystal growth, electronic cooling equipment, etc. Free or mixed convection in an enclosure

[a] e-mail: muthtamil1@buc.edu.in

influenced by the magnetic field has been performed [1–6]. Nanofluids, introduced by Choi and Estman [7], dispersing ultrafine metallic particles into the base fluids, have focused in the convective heat transfer processes. The reason is that the nanofluids have superior thermal conductivity than the conventional fluids. Some numerical simulations related to combined convection in a nanofluid filled lid-driven enclosure are listed in the references [8–12]. The problem of heat transfer in a porous cavity has been the most important topic in convectional heat transfer due to its wide spectrum of many engineering applications. Numerical investigation on mixed convective heat transfer in a porous enclosure with moving lid(s) has been discussed [13–18]. Recently, convection in a cavity filled with nanofluid saturated porous medium has received much popularity among the researchers on application to challenges prevailing in engineering problems. An investigation of heat transfer in an enclosure or a plate with nanofluid saturated porous medium has been performed by some researchers [19–23].

In the current literature survey, study on momentum and energy transfer is discussed into four groupings classes, for instance convection flow of an electrically conducting fluid, mixed convection flow in an enclosure filled with nanofluid, natural or combined convection flow in a porous cavity and mixed convection in a cavity or a plate nanofluid saturated porous medium. On the other hand, there is no study combining the above four categories. Further, in many engineering applications, the physical system is designed not only in the square type but also in the rectangular shape. Therefore, the above observations motivate the present study to analyze the influence of tilted Lorentz force on both free and forced convective heat transfer in a 2-D rectangular enclosure filled with nanofluid saturated porous medium. Especially, this investigation aims to discuss numerically the impacts of tilted angles of magnetic field and aspect ratio with respct to Darcy number, Hartmann number and the solid volume fraction. With respect to the above literature review and to the author's preposition there is no such investigation initiated so far.

2 Mathematical analysis

A physical configuration of the present analysis, mixed convection in a 2-D rectangular porous enclosure of length L and height H filled with nanofluid is presented in Figure 1. x and y axes represent the dimensional velocity components u and v respectively. The vertical walls of the cavity are considered to be adiabatic. The upper and lower horizontal walls are fixed at temperatures θ_h and θ_c on the condition that $\theta_h > \theta_c$. The top wall moves in its own plane from left to right at constant velocity U_0. The cavity is filled with Cu-water nanofluid saturated porous medium. The flow inside the cavity is considered to be steady, laminar, incompressible and Newtonian. No slip condition is assumed between the fluid and two vertical walls. Further, the tangential fluid velocity is considered as equal to the moving wall velocity. The nanoparticle size and shape are uniform and no slip velocity occurs between the base fluid and nanoparticles. Base fluid and nanoparticles are in thermal equilibrium. Barring density, the thermo-physical properties of the nanofluid remain constant due to Boussinesq approximation, as listed in Table 1. A magnetic field with magnitude B_0 is applied parallel to the horizontal walls uniformly. The slope of the applied magnetic field is γ. The porous medium is uniform and hydro-dynamically and thermally isotropic. The local thermal equilibrium (LTE) conditions exist between porous medium and nanofluid. Further, it is considered that the Joule heating effect, induced magnetic field effect, viscous dissipation and internal heat generation are trivial. The subscripts f, s, nf, nl, eq and eff are stand for fluid, solid, nanofluid, nanolayer,

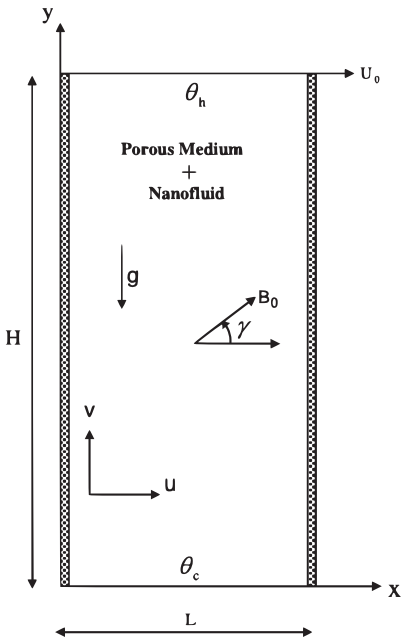

Fig. 1. Physical diagram of the considered study.

Table 1. Thermo-physical properties of base fluid and nanoparticles [19,21].

	ρ (kgm^{-3})	C_p(Jkg^{-1}K^{-1})	k(Wm^{-1}K^{-1})	$\beta \times 10^{-5}$(K^{-1})
Water	997.1	4179	0.613	21
Copper(Cu)	8933	385	401	1.67

equivalent and effective respectively. The non-dimensional form of governing equations for the above assumptions as follows:

$$\frac{\partial U}{\partial X} + \frac{\partial V}{\partial Y} = 0 \tag{1}$$

$$\begin{aligned}\frac{1}{\epsilon^2}\left(U\frac{\partial U}{\partial X} + V\frac{\partial U}{\partial Y}\right) &= -\frac{\rho_f}{\rho_{\rm nf}}\frac{\partial P}{\partial X} + \frac{\mu_{\rm nf}}{\epsilon Re \rho_{\rm nf}\nu_f}\left(\frac{\partial^2 U}{\partial X^2} + \frac{\partial^2 U}{\partial Y^2}\right) - \frac{\mu_{\rm nf}}{\rho_{\rm nf}\nu_f}\frac{U}{ReDa} \\ &\quad - \frac{1.75}{\sqrt{150}}\frac{(U^2+V^2)^{1/2}}{\sqrt{Da}}\frac{U}{\epsilon^{3/2}} \\ &\quad + \frac{\sigma_{\rm nf}}{\sigma_f}\frac{\rho_f}{\rho_{\rm nf}}\frac{Ha^2}{Re}[V\sin(\gamma)\cos(\gamma) - U\sin^2(\gamma)]\end{aligned} \tag{2}$$

$$\begin{aligned}\frac{1}{\epsilon^2}\left(U\frac{\partial V}{\partial X} + V\frac{\partial V}{\partial Y}\right) &= -\frac{\rho_f}{\rho_{\rm nf}}\frac{\partial P}{\partial Y} + \frac{\mu_{\rm nf}}{\epsilon Re \rho_{\rm nf}\nu_f}\left(\frac{\partial^2 V}{\partial X^2} + \frac{\partial^2 V}{\partial Y^2}\right) - \frac{\mu_{\rm nf}}{\rho_{\rm nf}\nu_f}\frac{V}{ReDa} \\ &\quad - \frac{1.75}{\sqrt{150}}\frac{(U^2+V^2)^{1/2}}{\sqrt{Da}}\frac{V}{\epsilon^{3/2}} + \frac{(\rho\beta)_{\rm nf}}{\rho_{\rm nf}\beta_f}(RiT) \\ &\quad + \frac{\sigma_{\rm nf}}{\sigma_f}\frac{\rho_f}{\rho_{\rm nf}}\frac{Ha^2}{Re}[U\sin(\gamma)\cos(\gamma) - V\cos^2(\gamma)]\end{aligned} \tag{3}$$

$$U\frac{\partial T}{\partial X} + V\frac{\partial T}{\partial Y} = \frac{\alpha_{\rm nf}}{\alpha_f}\frac{1}{PrRe}\left(\frac{\partial^2 T}{\partial X^2} + \frac{\partial^2 T}{\partial Y^2}\right) \tag{4}$$

along with the temperature and velocity conditions at boundaries:

$$U = 1, V = 0, \qquad T = 1, \quad Y = Ar$$
$$U = V = 0, \qquad T = 0, \quad Y = 0$$
$$U = V = 0, \qquad \frac{\partial T}{\partial X} = 0, \quad X = 0, X = Ar$$

where X, Y, U, V, T and P are the dimensionless form of the dimensional quantities x, y, u, v, θ and p respectivly and they are defined as $X = x/H$, $Y = y/H$, $U = u/U_0$, $V = v/U_0$, $T = (\theta - \theta_c)/(\theta_h - \theta_c)$ and $P = p/\rho U_0^2$. Based on Ergun's [24] formula, the Forchheimer's coefficient F and the permeability of the porous medium K are calculated as follows

$$F = \frac{1.75}{\sqrt{150}\epsilon^{3/2}}; \qquad K = \frac{\epsilon^2 d_p^2}{150(1-\epsilon)^2}$$

where d_p is the size of the average particle and ϵ is the porosity.

Further, the dimensionless parameters appeared in equations (1)–(4) are Hartmann number $Ha^2 = \sigma_f B_0^2 H^2/\mu_f$, Darcy number $Da = K/H^2$, Prandtl number $Pr = \nu_f/\alpha_f$, Reynolds number $Re = U_0 H/\nu_f$, Grashof number $Gr = g\beta\Delta\theta H^3/\nu_f^2$ and Richardson number $Ri = Gr/Re^2$, where ν, σ, μ, g and α are the kinematic viscosity, electrical conductivity, dynamic viscosity, gravitational acceleration and thermal diffusivity respectively.

The nanofluid properties effective density (ρ), the thermal diffusivity (α), the heat capacitance(ρC_p), the dynamic viscosity (μ) and the thermal expansion coefficient (β) are expressed by the following relations [8,11,19] and [21]:

$$\rho_{\rm nf} = (1-\chi)\rho_f + \chi\rho_s \tag{5}$$
$$\alpha_{\rm nf} = \frac{K_{\rm eff}}{(\rho C_p)_{\rm nf}} \tag{6}$$
$$(\rho C_p)_{\rm nf} = (1-\chi)(\rho C_p)_f + \chi(\rho C_p)_s \tag{7}$$
$$\mu_{\rm nf} = \frac{\mu_f}{(1-\chi)^{2.5}} \tag{8}$$
$$(\rho\beta)_{\rm nf} = (1-\chi)\rho_f\beta_f + \chi\rho_s\beta_s. \tag{9}$$

Nanofluid effective thermal conductivity for spherical nanoparticles $k_{\rm eff}$ is obtained by Modified Maxwell [25] model as given below;

$$\frac{k_{\rm eff}}{k_f} = \frac{(k_{\rm eq} + 2k_f) + 2(k_{\rm eq} - k_f)(1+\omega)^3\chi}{(k_{\rm eq} + 2k_f) - (k_{\rm eq} - k_f)(1+\omega)^3\chi} \tag{10}$$

where $\omega = \frac{\text{thickness of nanolayer}(h_{\rm nl})}{\text{radius of nanoparticles}(r_s)}$ and the nanoparticles equivalent thermal conductivity $k_{\rm eq}$ is described as follows;

$$\frac{k_{\rm eq}}{k_s} = \eta\frac{2(1-\eta) + (1+\omega)^3(1+2\eta)}{-(1-\eta) + (1+\omega)^3(1+2\eta)}. \tag{11}$$

In this equation, $\eta = \frac{k_{\rm nl}}{k_s}$. In the present study, it is considered that the nanolayer thickness, nanoparticles radius and the nano-layer thermal conductivity($k_{\rm nl}$) are 2 nm, 3 nm and $100k_f$ respectively. Also, the fraction of solid volume is represented by χ. Yu and Choi [26] tested the results of modified Maxwell model experimentally for the above conditions and found the results to be in good agreement.

The local Nusselt number (Nu) and the average Nusselt number ($Nu_{\rm avg}$) for obtaining the rate of heat transfer inside the enclosure are calculated as follows;

$$Nu = -\frac{K_{\rm eff}}{K_f}\frac{1}{Ar}\frac{\partial T}{\partial Y} \tag{12}$$

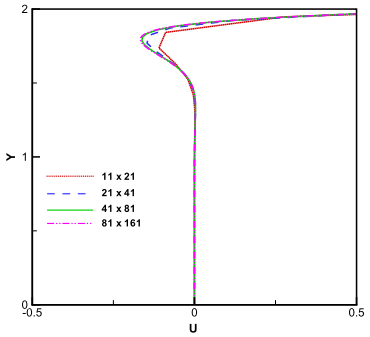

Fig. 2. Mid-plane U-velocity profile for different mesh sizes at $Ar = 0.5$, $Ri = 1$, $\gamma = 0°$, $Ha = 50$, $Da = 10^{-2}$, $\epsilon = 0.4$ and $\chi = 0.06$.

and

$$Nu_{\text{avg}} = \int_0^{Ar} Nu \; dX. \tag{13}$$

3 Numerical technique and validation of algorithm

The non-dimensional equations (1)–(4) are solved by finite volume method (FVM) to obtain the numerical solutions. The grid selection is uniform in both X and Y directions. By using Patankar's [27] SIMPLE algorithm, pressure and velocity terms are paired. The third order accurate deferred QUICK scheme of Hayase et al. [28] is used to compute the convection fluxes at the inner nodes, whereas diffusion fluxes are calculated at the boundary nodes by using central differencing scheme in both momentum and energy equations. The non-dimensional equations are integrated over each control volumes. Tri-diagonal matrix algorithm line-by-line method is applied to solve the system of resultant equations. A grid independence checking is performed for the following range of grid sizes from 11×21 to 81×161 at $Ri = 1$, $Da = 10^{-2}$, $Ha = 50$, $Pr = 6.2$, $Ar = 0.5$, $\gamma = 0°$, $\epsilon = 0.4$, and $\chi = 0.06$ so as to regulate the suitable grid size for numerical calculations. Figure 2 illustrates the mid plane U-velocity profile for various grid sizes and it concludes that a 41×81 grid size is sufficient to get the preferred accuracy of results. Also, to assess the accurateness of the current numerical results, the validation of the developed programming code is performed by comparing it with that of in published works. The present code is tested with the simulation for mixed convection in porous enclosure numerically of Khanafer and Chamka [29]. The comparison results are depicted in Figure 3 for different Darcy numbers $Da = 10^{-3}$ and $Da = 10^{-2}$ at $Ri = 10^{-2}$. It shows an excellent concurrence between the two numerical results. Moreover, the current code is validated with the results of Iwatsu et al. [30]. Figure 4 shows the streamlines and isotherms for $Re = 10^3, Gr = 10^2$ and $Pr = 0.71$. There is a clear agreement between the two numerical simulations.

4 Results and discussion

A numerical investigation is carried out to examine the impact of magnetic field slanting angles on mixed convection flow of nanofluid in a two dimensional lid-driven rectangular porous enclosure. The moving top wall is heated with uniform temperature whereas the bottom wall remains at a constant cold temperature. Thermally

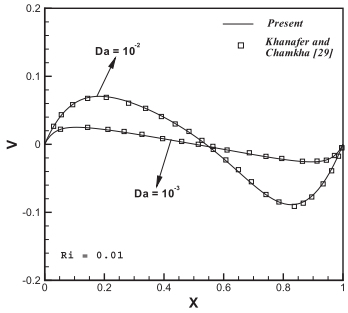

Fig. 3. Comparison of the mid-plane V-velocity with the results of Khanafer and Chamka [29].

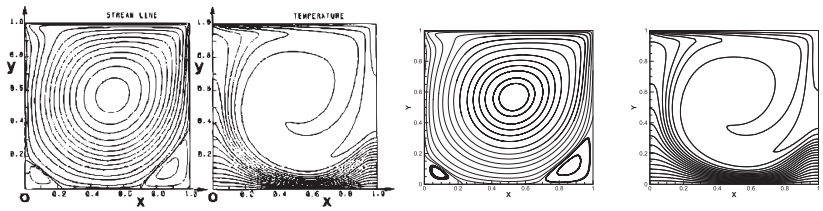

(a) Iwatsu et al.[30] (b) Present study

Fig. 4. Comparison of Streamlines and Isotherms with the results of Iwatsu et al. [30] at $Re = 10^3$, $Gr = 10^2$ and $Pr = 0.71$.

insulated walls are fixed at the left and right sides of the cavity. The Prandtl number of working nanofluid Cu-water is fixed as 6.2. The porosity of the porous medium is chosen as $\epsilon = 0.4$, in this analysis entirely. Streamlines, temperature contours, velocity profiles and average Nusselt number are used to discuss the obtained results for a mixture of the following parameters Richardson number ($0.01 \leq Ri \leq 100$), the solid volume fraction ($0.00 \leq \chi \leq 0.06$), Darcy number ($10^{-4} \leq Da \leq 10^{-1}$), Hartmann number ($0 \leq Ha \leq 70$) and the slope of magnetic field ($0° \leq \gamma \leq 90°$). Further, the aspect ratio Ar varies from 0.25 to 2 which is measured as the ratio of length (L) and height (H).

4.1 Effects of magnetic field inclination with different aspect ratios

To examine the influence of aspect ratio and magnetic field slanting angle at $Ri = 0.01$, the other parameters are chosen as $Ha = 50, Da = 10^{-2}$ and $\chi = 0.06$ and the results are described in Figures 5–8. Figure 5 presents the temperature contours and flow patterns for different magnetic field inclinations at $Ar = 0.25$. For $\gamma = 0°$, the applied magnetic field stimulates Lorentz force which acts normal to the direction of applied magnetic field vector. As a result, a three-cellular flow structure exists at the top most half of the cavity and the nanofluid is almost stagnant in the lower part of the cavity. The corresponding isotherms are distributed in the upper component of the cavity and the temperature gradients are high nearer the right vertical wall due to intense effect of the moving lid. Conduction mode of heat transfer exists. When the horizontal direction of the applied magnetic field deviates to vertical direction, the fluid flow pattern and heat transfer characteristics in the enclosure are influenced. When $\gamma = 90°$, the Lorentz force acts parallel to the moving hot wall and enhances the shear force. Hence, three cells get merged and a single clockwise (CW) rotating vortex occupies the whole cavity. The core region of the cell is located near the top

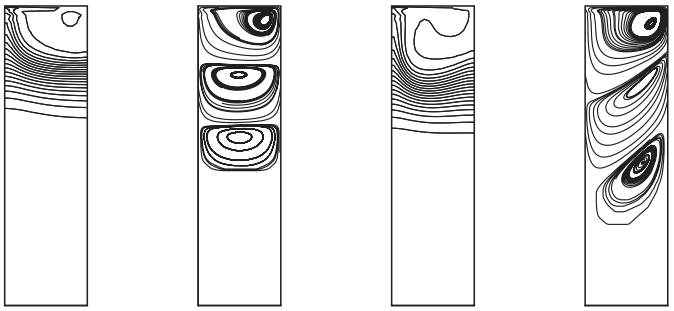

(a) $\gamma = 0^0$ (b) $\gamma = 30^0$

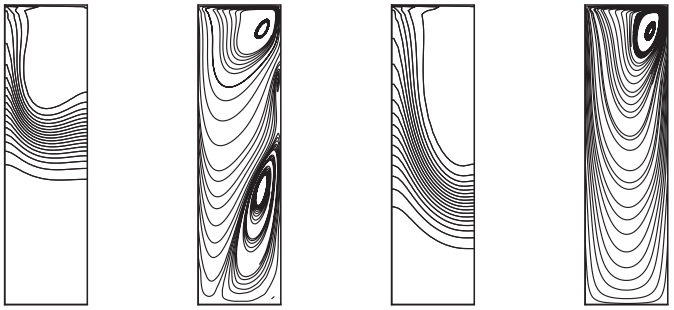

(c) $\gamma = 60^0$ (d) $\gamma = 90^0$

Fig. 5. Isotherms and Streamlines for different inclination angles of magnetic field with $Ri = 0.01$, $Da = 10^{-2}$, $Ar = 0.25$, $\chi = 0.06$ and $Ha = 50$.

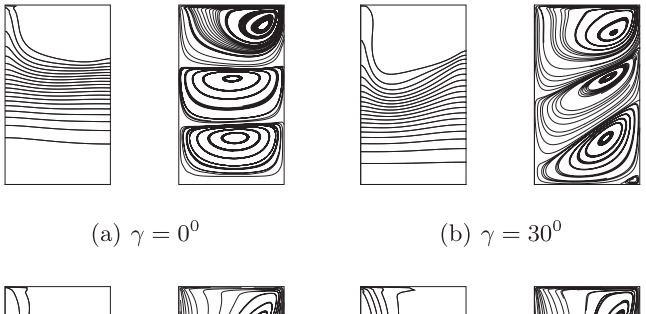

(a) $\gamma = 0^0$ (b) $\gamma = 30^0$

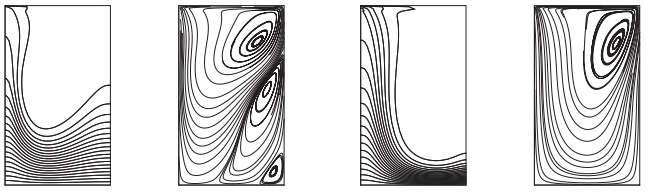

(c) $\gamma = 60^0$ (d) $\gamma = 90^0$

Fig. 6. Isotherms and Streamlines for different inclination angles of magnetic field with $Ri = 0.01$, $Da = 10^{-2}$, $Ar = 0.5$, $\chi = 0.06$ and $Ha = 50$.

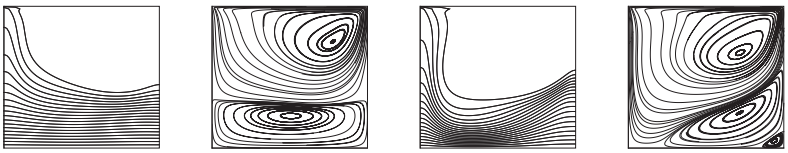

(a) $\gamma = 0^0$ (b) $\gamma = 30^0$

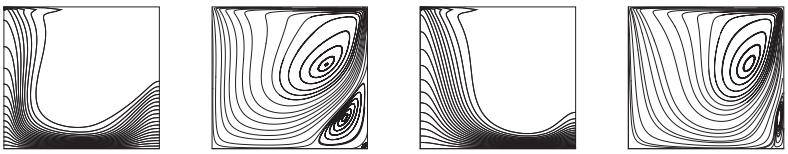

(c) $\gamma = 60^0$ (d) $\gamma = 90^0$

Fig. 7. Isotherms and Streamlines for different inclination angles of magnetic field with $Ri = 0.01$, $Da = 10^{-2}$, $Ar = 1$, $\chi = 0.06$ and $Ha = 50$.

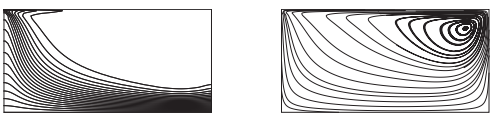

(a) $\gamma = 0^0$

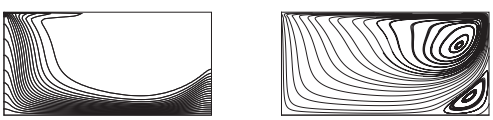

(b) $\gamma = 30^0$

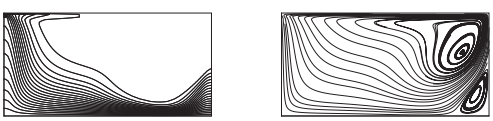

(c) $\gamma = 60^0$

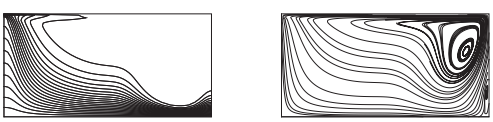

(d) $\gamma = 90^0$

Fig. 8. Isotherms and Streamlines for different inclination angles of magnetic field with $Ri = 0.01$, $Da = 10^{-2}$, $Ar = 2$, $\chi = 0.06$ and $Ha = 50$.

right corner of the cavity. The isotherms are pushed and expanded towards the cold bottom wall. The effects of different slopes of magnetic field on thermal pattern and fluid flow are shown in Figure 6 for $Ar = 0.5$. At $\gamma = 0°$, the cavity is filled with three vortices one below the other. The temperature contours are nearly parallel to the

horizontal wall illustrating conduction dominant heat transfer. Figure 6c exhibits the effect of magnetic field aligned angle at $\gamma = 60°$. The vertices are stretched diagonally towards a cold wall and the top vortex squeezes the other vortices. The isotherms at the center of the cavity become parabolic and the convection dominates over the conduction. As the inclination angle is increased to $\gamma = 90°$, a single CW rotating eddy fills the whole cavity. The temperature contours are crowded at the right bottom of the cavity.

The effect of magnetic field inclinations on fluid flow and isotherms in a square cavity ($Ar = 1$) is displayed in Figure 7. When $\gamma = 0°$, a large CW rotating eddy above a small CCW rotating eddy jointly occupy the whole enclosure. The corresponding isotherms appear nearly parallel to the bottom wall at the lower part of the cavity. Due to the vigorous effect of moving lid, small temperature differences stay alive at the upper component of the cavity. The large CW rotating eddy is elongated towards the bottom wall further and fills the entire cavity with a tiny cell nearer to the lower right wall of the enclosure as the slope of magnetic field increases from 0° to 90°. Moreover, as shown in Figure 6, the same result is also noticed on temperature contour maps with the raising of magnetic field tilting angle. The temperature contours and flow patterns for different magnetic field orientations with $Ar = 2$ are shown in Figure 8. In this case, thermally active wall becomes very closer to the cold wall and the length of the heating wall also increases. As a result, the effect of shear and buoyancy forces is more effective in high aspect ratio than that of in the low aspect ratios. When $\gamma = 0°$, the flow is exemplified by a major CW turning vortex caused by the moving lid. The distributions of isotherms are noticed mostly in the left part of the enclosure due to potent effect of moving top wall. Tilting the applied magnetic field by 30°, a small vortex occurs at the lower right part of the cavity and the core region of the major vortex moves downward. However, for $\gamma = 90°$, the major cell fills the whole cavity with a little cell at lower part of the right wall. Owing to the strong effect of shear force, the isotherms are crowded near the bottom wall and the small temperature gradients exist in the core region of the cavity.

Figure 9 illustrates the variations of mid-plane velocities with different aspect ratios and magnetic field inclination angles. When $Ar = 0.25$, the magnitude of U-velocity reduces with the increase in slope of magnetic field while it augments first and then decreases with a raise in the slope of magnetic field for the aspect ratios 0.5, 1 and 2. The cause of the above effect was to the closeness between the heated top wall and the cooled bottom wall as the value of the aspect ratio increases. For all considered Ar, an enhancement in the magnetic field tilting angle results an increase in the net value of V-velocity. The maximum of V-velocity occurs nearer to the lower part of the right wall owing to the mechanical effect of moving lid. The correlation on heat transfer rate for various aspect ratios and inclination angles of the magnetic field is demonstrated in Figure 10. It can be observed that in the forced convection regime, the slope of applied magnetic field has less effect when $Ar = 0.25$ whereas, it produces significant differences in the mean Nusselt number for the aspect ratios greater than 0.25. The maximum heat transfer takes place at $\gamma = 30°$ in the shallow cavity. The value of mean Nusselt number augments with the tilting angle of magnetic field for $Ar = 0.5$ and 1, though it increases first and then, decreases slightly for $Ar = 2$. The identical impact is noticed on the average Nusselt number too with the inclination angles of magnetic field and aspect ratios in $Ri = 1$ as in $Ri = 0.01$. For all considered aspect ratios, the slope of magnetic field is inactive in the dominant natural convection. Generally, the overall rate of heat transfer is decreased with enhancing in the Richardson number and the highest heat transfer takes place in the shallow enclosure.

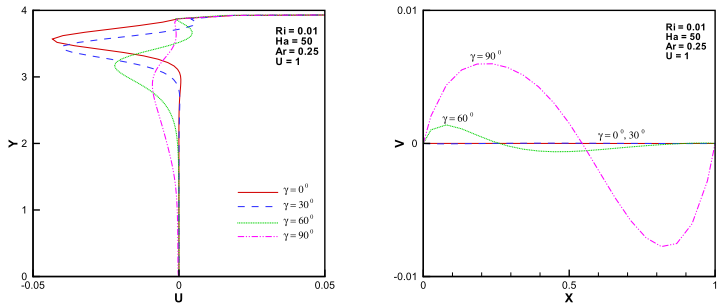

(a) $Ar = 0.25$

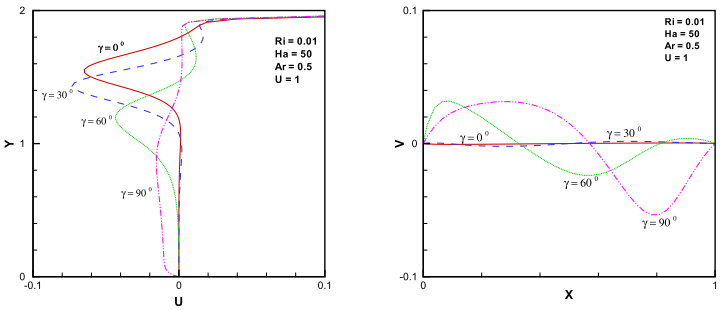

(b) $Ar = 0.5$

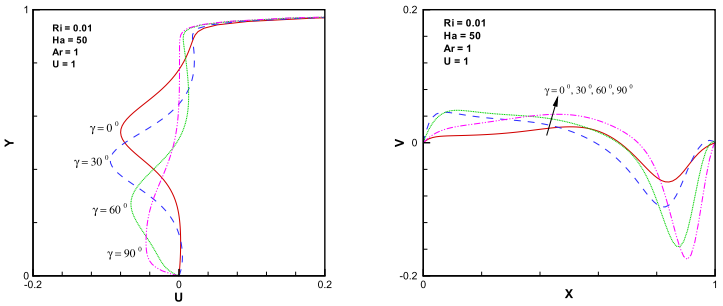

(c) $Ar = 1$

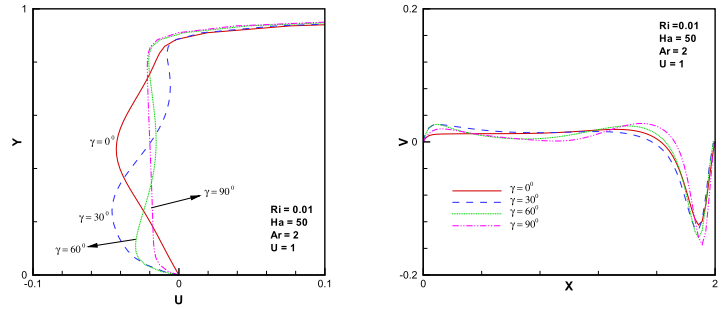

(d) $Ar = 2$

Fig. 9. U and V-velocity profiles for different inclination angles of magnetic field and aspect ratios with $Ri = 0.01$, $Da = 10^{-2}$, $\chi = 0.06$ and $Ha = 50$.

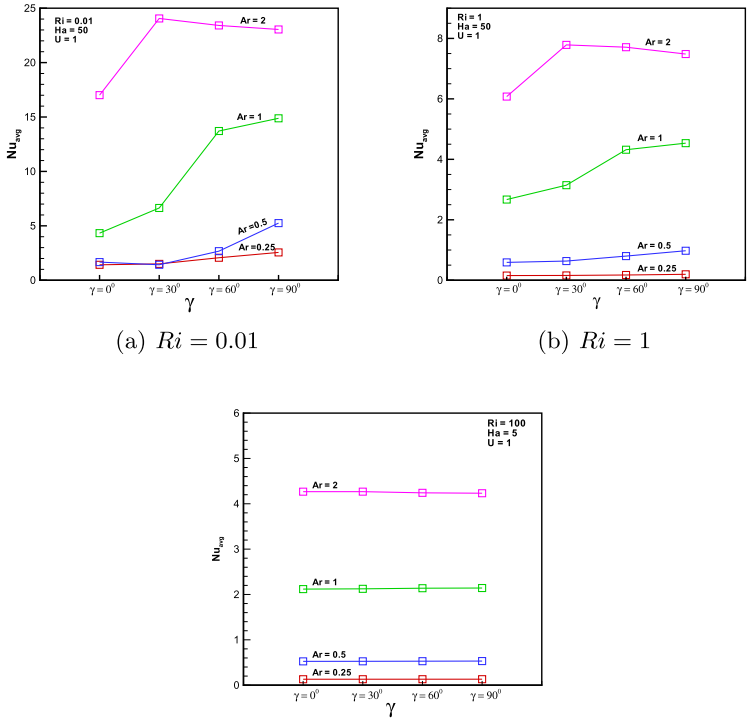

(a) $Ri = 0.01$ (b) $Ri = 1$

(c) $Ri = 100$

Fig. 10. Average Nusselt numbers for different inclination angles of magnetic field, aspect ratios and Richardson numbers with $Da = 10^{-2}$, $\chi = 0.06$ and $Ha = 50$.

4.2 Effects of magnetic field parameter

In order to investigate the influence of magnetic field parameter Ha, the other parameters are fixed as $Ri = 1$, $Da = 10^{-2}$, $\chi = 0.06$ and $\gamma = 0°$. Figure 11 represents the influence of Hartmann numbers on thermal field and fluid flow for $Ar = 0.5$. In the system without magnetic field, the fluid flow is marked by a primary CW rotating vortex and a secondary CCW rotating vortex at the upper and lower parts of the cavity. The isotherms resemble that conduction heat transfer exists at the lower part of the cavity and induced convective activities are considerable at the upper part of the cavity. On increasing the value of Ha from 0 to 20, Lorentz force inhibits the fluid flow. Thus, the bi-cellular flow formation is vanished and tri-cellular flow pattern appears inside the enclosure. The isotherms are uplifted towards the top wall. When $Ha = 70$, the flow is exemplified by multiple vortices one below the other and the nanofluid is almost inactive adjacent to the bottom cold wall. The heat transfer inside the cavity is the main means of conduction. The temperature contours and streamlines for different Hartmann numbers with $Ar = 2$ are shown in Figure 12. For $Ha = 0$, a large CW circulating vortex with a small CCW circulating vortex at the lower left part of the cavity exist. The cause of mechanically driving lid, the isotherms are clustered at lower right part of the enclosure. The temperature differences are small at the upper right part of the cavity and convection is the primary means of heat transfer. As Ha increases, the effect of the moving lid reduces while the magnetic field effect increases significantly. Accordingly, small vortex increases in its size and squeezes the primary vortex. Each vortex occupies each half of the cavity and the center of the primary eddy moves nearer to the moving wall. The isotherm contours

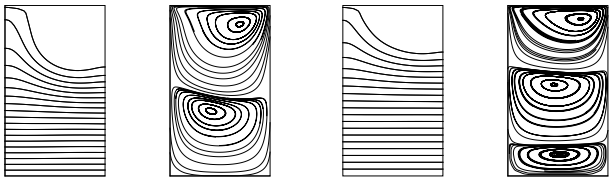

(a) $Ha = 0$ (b) $Ha = 20$

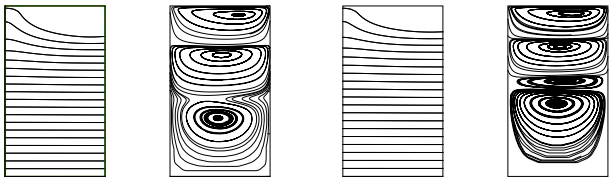

(c) $Ha = 50$ (d) $Ha = 70$

Fig. 11. Isotherms and Streamlines for different Hartmann numbers with $Ri = 1$, $Ar = 0.5$, $Da = 10^{-2}$, $\chi = 0.06$ and $\gamma = 0°$.

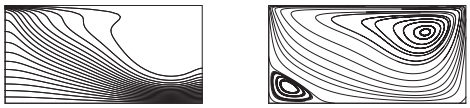

(a) $Ha = 0$

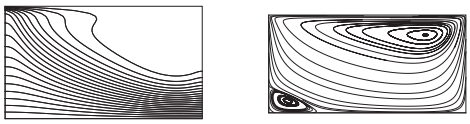

(b) $Ha = 20$

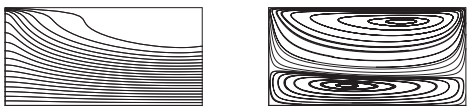

(c) $Ha = 50$

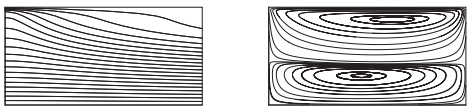

(d) $Ha = 70$

Fig. 12. Isotherms and Streamlines for different Hartmann numbers with $Ri = 1$, $Ar = 2$, $Da = 10^{-2}$, $\chi = 0.06$ and $\gamma = 0°$.

are uplifted and spread over the whole cavity. This shows that the conduction plays a major role in the presence of strong magnetic field.

The impact of the Hartmann number on the velocity profile at mid section of the rectangular cavity is displayed in Figure 13. For $Ar = 0.5$, an increase in Ha leads to increase in the magnitude of U-velocity in the upper part of the cavity and reduce

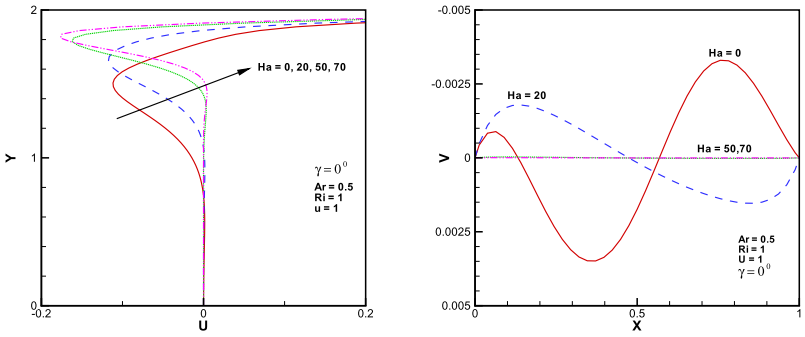

(a) $Ar = 0.5$

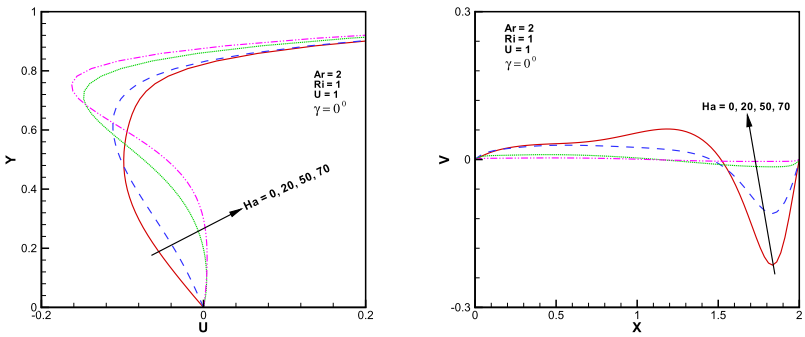

(b) $Ar = 2$

Fig. 13. U and V-velocity profiles for different Hartmann numbers and aspect ratios with $Ri = 1$, $Da = 10^{-2}$, $\chi = 0.06$ and $\gamma = 0°$.

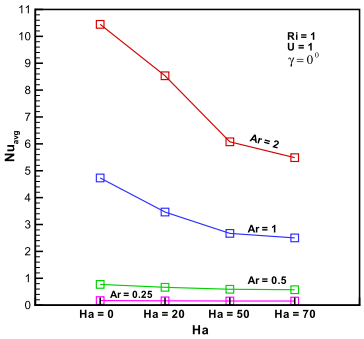

Fig. 14. Average Nusselt number for different Hartmann numbers and aspect ratios with $Ri = 1$, $Da = 10^{-2}$, $\chi = 0.06$ and $\gamma = 0°$.

in the magnitude of V-velocity in the whole cavity. For $Ar = 2$, the net U-velocity increases in the upper part of the cavity whereas it decreases in the lower part of the cavity with an increase in the Ha. Contrastingly, the net V-velocity decreases in the enclosure. Figure 14 illustrates the variation on the mean Nusselt number for different Hartmann numbers and aspect ratios. The mean Nusselt number diminishes with increased Ha and the diminishing rate is high for the aspect ratio 2. This effect is the cause that the heat transfer behavior within the enclosure happens almost convection mode when $Ha = 0$ while conduction exists with increasing the value of

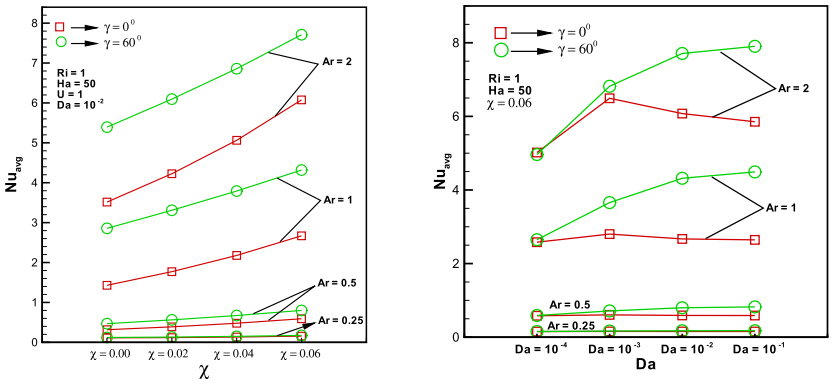

(a) χ (b) Da

Fig. 15. Average Nusselt number for different (a) solid volume fractions and (b) Darcy numbers with $Ri = 1$ and $Ha = 50$.

Ha. At *Ar* 0.25 and 0.5, the overall heat transfer rate is almost constant for all the considered values of Hartmann number. Consequently, the effect of applied magnetic is insignificant in the slender cavity.

4.3 Effects of Darcy number and solid volume fractions

Figure 15a is plotted to observe the effects of solid volume concentration of nanoparticles on the heat transfer rate with different aspect ratio at $Ri = 1$, $Ha = 50$ and $Da = 10^{-2}$. The average Nusselt number is raised linearly with respect to the augmentation in the solid volume fraction for $Ar > 0.25$ regardless of the magnetic field inclinations. Furthermore, a raise in the solid volume fraction has no notable effects on average Nusselt number at $Ar = 0.25$. The effect on the mean Nusselt number for various Da and Ar at $Ri = 1$, $Ha = 50$ and $\chi = 0.06$ is shown in Figure 15b. No considerable effect in the overall heat transfer rate is observed in the slender cavity with increasing Darcy number when$\gamma = 0°$. Meanwhile, the average Nusselt number increases first and then reduces as Da enhances for the aspect ratios 1 and 2. At the low permeability of porous medium $Da = 10^{-4}$, the effect of magnetic field inclination is not observed for all considered aspect ratios.

5 Conclusion

The influence of magnetic field inclinations and aspect ratio on combined convective heat transfer in a lid-driven porous cavity saturated with nanofluid is discussed in the present numerical investigation. The moving top wall is heated with uniform temperature whereas the bottom wall remains at a constant cold temperature. Thermally insulated walls are fixed at the left and right side of the cavity. The following conclusions are drawn from the obtained results. The mean Nusselt number increases with decreased Richardson number. The overall rate of heat transfer raises with an increase of aspect ratio in the nanofluid saturated porous cavity under the influence of magnetic field. The impact of applied magnetic field inclinations on the overall heat transfer rate is considerable when $Ri = 0.01$ and $Ri = 1$ while it is insignificant at $Ri = 100$. The average Nusselt number reduces considerably with the raise of Hartmann number in square and shallow cavity at $Ri = 1, Da = 10^{-2}$, $\chi = 0.06$ and

$\gamma = 0°$. However, an increase in Ha has no significant outcome on the overall rate of heat transfer for $Ar \leq 0.5$. An increase in the Hartmann number and the magnetic field tilting angles affect the fluid velocity inside the porous cavity. For $Ri = 1$, the net heat transfer rate is almost equal to the effect of solid volume fraction at $Ar = 0.25$ whether the magnetic field inclination is considered or not. The average Nusselt number increases on raising the solid volume fraction for aspect ratio 0.25. The impact of magnetic field inclination is insignificant at $Da = 10^{-4}$. The average Nusselt number is nearly invariable with the increase in Darcy number for $Ar \leq 0.5$.

This research was supported by Basic Science Research Program through the National Research Foundation of Korea (NRF) funded by the Korea Government (No.2017R1A2B2010603) and (2018R1A2B6009387). This has been also supported by the Program of Business Cooperative R&D (R0006261) funded by MOTIE. This work was also supported by the Open Laboratory Operational Business Developing and Diffusing the Regional Specialization Technology funded by the Busan Institute of S&T Evaluation and Planning (B0060327000771).

Author contribution statement

S.S., S.M. and C.R.C. performed the mathematical formulations and numerical computations. M.M., D.H.D., and E.P. refined the analysis and figures. All authors discussed the results and contributed to the final manuscript.

References

1. I.E. Sarris, S.C. Kakarantzas, A.P. Grecos, N.S. Vlachos, Int. J. Heat Mass Transfer **48**, 3443 (2005)
2. J.M. Jalil, K.A. Al-Tae'y, Numer. Heat Transfer Part A **51**, 899 (2007)
3. G.R. Kefayati, M. Gorji-Bandpy, H. Sajjadi, D.D. Ganji, Sci. Iran. **19**, 1053 (2012)
4. S. Ray, D. Chatterjee, Int. Commun. Heat Mass Transfer **57**, 200 (2014)
5. S. Ray, D. Chatterjee, Numer. Heat Transfer Part A **66**, 530 (2014)
6. A. Malleswaran, S. Sivasankaran, J. Appl. Fluid Mech. **9**, 311 (2016)
7. S.U. Choi, J.A. Estman, ASME Publ. Fed. **48**, 99 (1995)
8. R.K. Tiwari, M.K. Das, Int. J. Heat Mass Transfer **50**, 2002 (2007)
9. M. Alinia, D.D. Ganji, M. Gorji-Bandpy, Int. Commun. Heat Mass Transfer **38**, 1428 (2011)
10. S.M. Aminossadati, A. Kargar, B. Ghasemi, Int. J. Therm. Sci. **52**, 102 (2012)
11. A. Fereidoon, S. Saedodin, M. Hemmat Esfe, M.J. Noroozi, Eng. Appl. Comput. Fluid Mech. **7**, 55 (2013)
12. M.H. Esfe, M. Akbari, D.S. Toghraie, A. Karimipour, M. Afrand, Heat Transfer Res. **45**, 409 (2014)
13. K. Khanafer, K. Vafai, Numer. Heat Transfer Part A **42**, 465 (2002)
14. I.A. Badruddin, Z.A. Zainal, P.A. Aswatha Narayana, K.N. Seetharamu, Int. Commun. Heat Mass Transfer **33**, 491 (2006)
15. E. Vishnuvardhanarao, M.K. Das, Numer. Heat Transfer Part A **53**, 88 (2007)
16. T. Basak, P.V. Krishna Pradeep, S. Roy, I. Pop, Int. J. Heat Mass Transfer **54**, 1706 (2011)
17. L. Agarwal, A.Satheesh, C.G. Mohan, Heat Transfer Asian Res. **44**, 305 (2015)
18. M.M. Rahman, H.F. Öztop, R. Saidur, S. Mekhilef, K. Al-Salem, Therm. Sci. **19**, 1761 (2015)
19. A.J. Chamkha, M.A. Ismael, Int. J. Therm. Sci. **67**, 135 (2013)
20. A.M. Rashad, A.J. Chamkha, C. RamReddy, P.V.S.N. Murthy, Heat Transfer Asian Res. **43**, 397 (2014)

21. A.A.Hassan, M.A. Ismael, Int. J. Therm. Env. Eng. **10**, 93 (2015)
22. S. Sureshkumar, M. Muthtamilselvan, Eur. Phys. J. Plus **131**, 95 (2016)
23. M. Muthtamilselvan, S. Sureshkumar, Nonlinear Eng. **7**, 1 (2018)
24. S. Ergun, Chem. Eng. Prog. **48**, 89 (1952)
25. J.C. Maxwel, in *A treatise on electricity and magnetism* (Oxford University Press, Cambridge, 1904), pp. 435–441
26. W. Yu, S.U. Choi, J. Nanopart. Res. **5**, 167 (2003)
27. S.V. Patankar, in *Numerical heat transfer and fluid flow* (McGraw Hill book company, New York, 1980), pp. 126–130
28. T. Hayase, J.A. Humphrey, R.A. Greif, J. Comput. Phys. **98**, 108 (1992)
29. K.M. Khanafer, A.J. Chamkha, Int. J. Heat Mass Transfer **42**, 2465 (1999)
30. R. Iwatsu, J.M. Hyun, K. Kuwahara, Int. J. Heat Mass Transfer **36**, 1601 (1993)